Journal of Alloys and Compounds 741 (2018) 442–448

Contents lists available at ScienceDirect

Journal of Alloys and Compounds

journal homepage: http://www.elsevier.com/locate/jalcom

Pseudocapacitive charge storage induced by self-enhanced electrical conductivity and Li-ion diffusion in high performance Li_3VO_4@$LiVO_2$ anode for Li-ion batteries

Tao Kang [a], Dongyang Shen [a], Shibing Ni [a, *], Qichang Chen [a], Tao Li [a], Xuelin Yang [a, **], Jinbao Zhao [b]

[a] College of Materials and Chemical Engineering, Hubei Provincial Collaborative Innovational Center for New Energy Microgrid, Key Laboratory of Inorganic Nonmetallic Crystalline and Energy Conversion Materials, China Three Gorges University, Yichang, 443002, China
[b] State Key Laboratory of Physical Chemistry of Solid Surfaces, Xiamen University, Xiamen 361005, PR China

ARTICLE INFO

Article history:
Received 6 December 2017
Received in revised form
8 January 2018
Accepted 9 January 2018
Available online 10 January 2018

Keywords:
Lithium vanadate
Pseudocapacitive
Composite material
Anode

ABSTRACT

Li_3VO_4@$LiVO_2$ composite with a specific architecture of Li_3VO_4 crystals homogeneously embraced by $LiVO_2$ matrix is fabricated via an intermediate solution approach with subsequent sintering. In the Li_3VO_4@$LiVO_2$, the small-sized Li_3VO_4 and the weak crystallized $LiVO_2$ render self-enhanced fast lithium ion diffusion and high electrical conductivity, which trigger high pseudocapacitive charge storage and result in superior cycle stability and rate capability. The Li_3VO_4@$LiVO_2$ delivers initial discharge and charge capacities of 569 and 448 mAh g^{-1} at a specific current of 0.15 A g^{-1}. The discharge and charge capacities exhibit no attenuation in cycling, maintaining at 468 and 471 mAh g^{-1} after 100 cycles. After 70 cycles at various specific currents from 0.1 to 2.0 A g^{-1}, the Li_3VO_4@$LiVO_2$ recovers high reversible capacity of 478 mAh g^{-1} when reverting the specific current to 0.1 A g^{-1}.

1. Introduction

In the past few decades, lithium ion batteries (LIBs) have become the dominant power sources for portable electronic devices owing to their high energy density, high power density, long cycle life and low cost [1]. Recently, they have also been intensively regarded as ideal power supplies for electric vehicles, hybrid electric vehicles and large-scale stationary energy storage [2]. One of the main tasks for LIBs is searching for graphite anode alternatives with higher specific capacity and safer lithiation potential [3,4], with these expected electrochemical properties for new anode materials further improving the energy density and safety performance of full cells when matching with cathode materials.

Among various new anode materials, Li_3VO_4 has been demonstrated as one of the most promising candidate for graphite, primarily due to: 1) it possess insertion/extraction mechanism which displays little volume variation upon lithiation/delithiation; 2) low but safe voltage for lithiation/delithiation (0.5–1 V vs. Li/Li^+) and 3) high theoretical capacity ~592 mAh g^{-1} [5]; However, pristine Li_3VO_4 usually suffers from low intrinsic electronic conductivity, and the reaction activity of Li_3VO_4 particles deteriorates sharply along with the increasing of particle size [6], resulting in unsatisfactory electrochemical performance in terms of specific capacity, cycle stability and rate capability. To address these problems, attempts have been tried mainly through four aspects. 1) enhancing the reaction activity via reducing the particle size of Li_3VO_4 or designing special morphologies with distinctly reduced diameter at one or two dimensions [7,8]; 2) improving the electronic conductivity via exteriorly combining Li_3VO_4 with carbonaceous materials such as graphite, carbon nanotubes, and graphene [9–13]; 3) in situ growing it on electric substrate [14,15]; 4) interiorly tuning the electrical properties through Mg or Mo doping [16,17] or creating defects such as oxygen vacancies [18]. Remarkably, hybridizing amorphous C within Li_3VO_4 particles has been proven effective to improving the specific capacity and cycle life of Li_3VO_4/C, because C nanonetwork in the Li_3VO_4/C can not only significant enhance the electron transfer process, but also effectively suppress the growth of Li_3VO_4 crystals which results in high lithium storage activity [5]. Nevertheless, much different physical and chemical properties of C and Li_3VO_4 will inevitably affect the hybridization degree and the

* Corresponding author.
** Corresponding author.
E-mail addresses: shibingni07@126.com (S. Ni), xlyang@ctgu.edu.cn (X. Yang).

https://doi.org/10.1016/j.jallcom.2018.01.129
0925-8388/

synergistic electrochemical effect between the two phases in the composite, resulting in limitations for controlled fabrication and practical application. Fortunately, an analog for Li_3VO_4, $LiVO_2$ which has been demonstrated to be of excellent ionic and electronic conductivity comes into the spotlight for hybridization with Li_3VO_4 [19,20].

Here in this paper, we report for the first time, significantly improving the performance of Li_3VO_4 via hybridizing with $LiVO_2$ analogs (Li_3VO_4@$LiVO_2$). In the composite, $LiVO_2$ acts as both conductive additive and particle growing inhibitor for Li_3VO_4, rendering self-enhanced electronic conductivity and lithium ion diffusion, which triggers high pseudocapacitive contribution for charge storage and results in superior performance.

2. Experimental

2.1. Fabrication procedure

The typical synthesis process of the Li_3VO_4/$LiVO_2$ was carried out as follows. In a procedure, 1 mmol V_2O_5, 3 mmol Li_2CO_3 and 5 mmol hexamethylenetetramine were added in 30 ml distilled water and stirred for 30 min until a homogeneous yellowy suspension was formed. After that, the mixed suspension was transferred into a 50 ml teflonlined autoclave, distilled water was subsequently added to 80% of its capacity. The autoclave was at last sealed and placed in an oven, heated at 120 °C for 24 h. The final transparent solution was transferred in a culture dish, additional 0.1 mmol NH_4VO_3 was introduced into the solution. After stirring for 2 h, the homogeneous solution was dried in an oven at 50 °C. At last, the precipitates were collected and sintered in N_2 atmosphere at 550 °C for 5 h.

2.2. Structural, morphological and electrical characterization

The structure and morphology of the resulting products were characterized by X-Ray powder diffraction (Rigaku Ultima IV Cu Kα radiation λ = 1.5406 Å), field-emission scanning electron microscopy (FE-SEM JSM 7500F, JEOL), transmission electron microscopy (TEM, FEI, Tecnai G2 F30). The electrical conductivity was investigated via a powder conductivity measurement system (FT-300I, Rico, China). Typically, 0.1 g powder sample was weighed and placed in a sample of the powder conductivity tester, then it was automatically compacted to form a column with thickness of ~1 mm for testing.

2.3. Electrochemical characterization

The electrochemical properties were evaluated by galvanostatic discharge/charge technique using two-electrode Coin-type cells. For the fabrication of lithium ion battery, a mixture of 80 wt% of active material, 10 wt% of acetylene black, and 10 wt% of polyvinylidene fluoride (PVDF) dissolved in N-methylpyrrolidine (NMP) solution (0.02 g mL^{-1}) were coated on copper foil and cut into disc electrodes with a diameter of 14 mm using a punch. Coin-type cells (2025) of Li/1 M $LiPF_6$ in ethylene carbonate, dimethyl carbonate and diethyl carbonate (EC/DMC/DEC, 1:1:1 v/v/v)/Li_3VO_4@$LiVO_2$ disc electrode were assembled in an argon-filled dry box (MIKROUNA, Super 1220/750, H_2O < 1.0 ppm, O_2 < 1.0 ppm). A Celgard 2400 microporous polypropylene was used as the separator membrane. The cells were tested in the voltage range between 0.02 and 3 V with a multichannel battery test system (LAND CT2001A). The Cyclic voltammetry (CV) measurement of the electrodes was carried out on a CHI660C electrochemical workstation at a scan rate of 0.2 mV s^{-1} between 0 and 3 V. Electrochemical impedance spectroscopy (EIS) measurements were performed on CHI660C electrochemical workstation under open circuit conditions over a frequency range from 0.01 Hz to 100 kHz by applying an AC signal of 5 mV in amplitude throughout the tests.

3. Results and discussion

Fig. 1(a) depicts XRD pattern of the as-prepared sample. As seen, sharp diffraction peaks located at 16.2°, 21.4°, 22.7°, 24.2°, 28.1°, 32.8°, 36.2°, 37.6°, 40.3°, 42.5°, 47.7°, 49.8°, 51.9°, 55.8°, 58.5°, 64.1°, 66.1°, 70.8° and 80.1° can be attributed to the (100), (110), (011), (101), (111), (200), (002), (201), (211), (112), (221), (131), (212), (311), (320), (141), (203), (322) and (151) faces of orthorhombic Li_3VO_4 with lattice constants a = 6.319 Å, b = 5.448 Å and c = 4.940 Å, which is in good agreement with JCPDS, no. 38-1247. In contrast, two broadened diffraction peaks (marked by ★) located at 18.0° and 43.9° can ascribe to $LiVO_2$ (JCPDS, no. 47-1182), suggesting lower crystallization degree. Typical Raman peaks (Fig. 1(b)) in the wavelength region 250–900 cm^{-1} are in accordance with those for Li_3VO_4 [12]. However, except for three clear peaks located at 776, 817 and 878 cm^{-1}, other peaks in wavelength region 250–450 cm^{-1} can not be distinctly distinguished. The merged Raman peaks consist with previous studies for Li_3VO_4/graphene and Li_3VO_4/C composites in which graphene and amorphous C exhibit homogeneous hybridization with Li_3VO_4 at

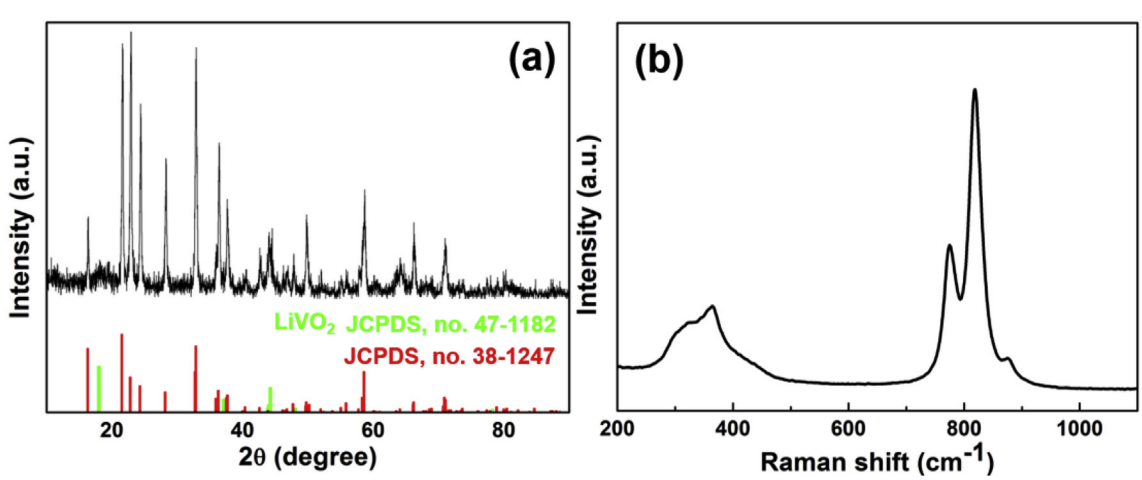

Fig. 1. XRD pattern (a) and Raman spectrum (b) of the obtained products.

nanoscale [5,9,12]. According to above results, it is safe to say that Li_3VO_4@$LiVO_2$ is successfully prepared.

Fig. 2(a) is a SEM image of the as-prepared Li_3VO_4@$LiVO_2$, which exhibits particle-like morphology with size distribution ranging from 500 nm to several micrometers. The microstructure of these Li_3VO_4@$LiVO_2$ particles was further studied via TEM and HRTEM. As shown in a TEM image in Fig. 2(b), the Li_3VO_4@$LiVO_2$ consists of numerous ultrafine nanoparticles with mean size of ~5 nm. Such microstructure of the Li_3VO_4@$LiVO_2$ is similar to that of Li_3VO_4@C where C hybridizes homogeneously within Li_3VO_4 particles and prevents the growth of Li_3VO_4 crystals, resulting in high electronic conductivity and high reaction activity. HRTEM image in Fig. 2(c) suggests the Li_3VO_4@$LiVO_2$ exhibits crystalline-amorphous architecture. Clear lattice fringes with interplanar spacing of 0.366 nm can attribute to the (101) planes of Li_3VO_4, whereas other phase with weak crystallization degree cannot be clearly distinguished. SAED pattern was employed to further confirm the composition of the Li_3VO_4@$LiVO_2$. As shown in Fig. 2(d), circular diffraction spots indicate the polycrystalline characteristic of the Li_3VO_4@$LiVO_2$. The (110), (111), (200) and (211) crystallographic planes for Li_3VO_4 can be identified, while the detailed crystallographic information for $LiVO_2$ is not very clear up to now.

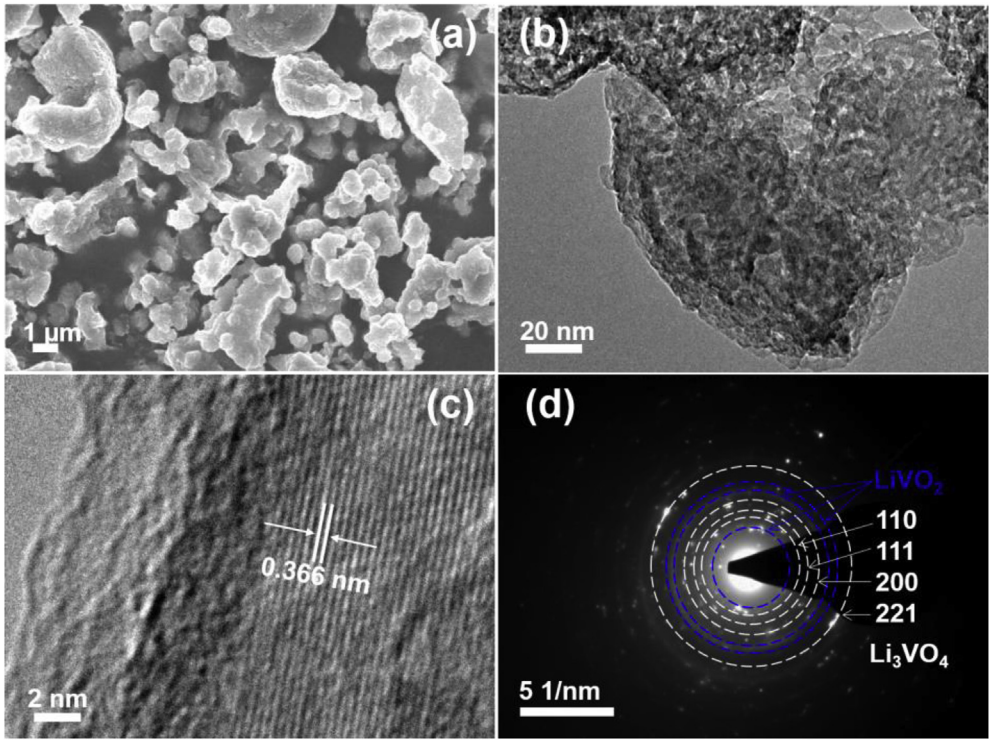

Fig. 2. (a) SEM, (b) TEM, (c) HRTEM images and (d) SAED pattern of the as-prepared Li_3VO_4@$LiVO_2$.

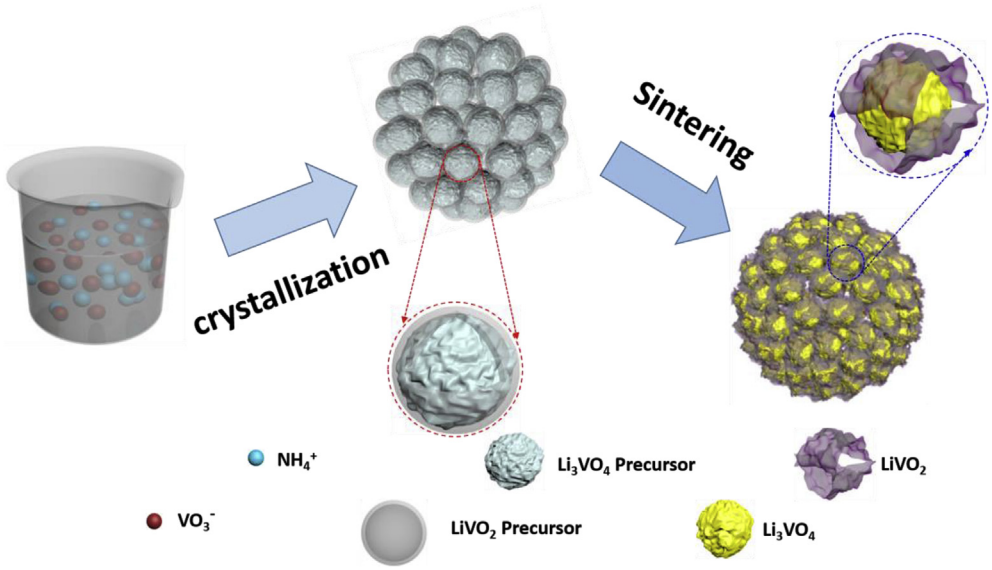

Fig. 3. Schematic illustration for the formation of Li_3VO_4@$LiVO_2$.

Based on above compositional and microstructural observations, a schematic for the formation of the Li_3VO_4@$LiVO_2$ is illustrated (Fig. 3). An intermediate solution phase obtained via hydrothermal reaction facilitates the dissolution and homogeneous distribution of NH_4VO_3, while nonstoichiometric ratio of Li:V (<1:3) induces the formation and crystallization of $LiVO_2$ and Li_3VO_4 precursors in heating process. Upon sintering, simultaneous solid state reactions for these precursors result in homogeneous hybridization between $LiVO_2$ and Li_3VO_4 at nanoscale.

The electrochemical performance of the Li_3VO_4@$LiVO_2$ was systematically assessed. Fig. 4(a) shows representative discharge/charge voltage profiles of the Li_3VO_4@$LiVO_2$ electrode at a current density of 0.15 A g^{-1} within a cut-off voltage window of 0.02–3.0 V. As seen, the initial discharge curve differs slightly from the subsequent ones, which shows two sloping potential regions 2.0–0.75 and 0.75–0.02 V, corresponding to the insertion of lithium ions into Li_3VO_4 and the formation of SEI [6–8,21]. From the second cycle onward, the discharge curves are similar in profile with two sloping potential regions (1.5–0.4 and 0.4–0.02 V). The charge curves exhibit similar profiles with a sloping potential region (0.6–2.5 V), which correspond to the extraction of lithium ions from $Li_{3+x}VO_4$ (x = 3) [6–8,21]. The cyclic voltammetric (CV) curves of the Li_3VO_4@$LiVO_2$ electrode were tested in voltage region 0–3.0 V at a scan rate of 0.2 mV s^{-1}. As shown in Fig. 4(b), the profiles of CV curves for the 2nd and 3rd cycle are similar, whereas an obvious difference between the first and the subsequent two cycles is found. In the 1st cathodic scan, three obvious reduction peaks at around 0.71, 0.52 and 0.35 V are observed, which

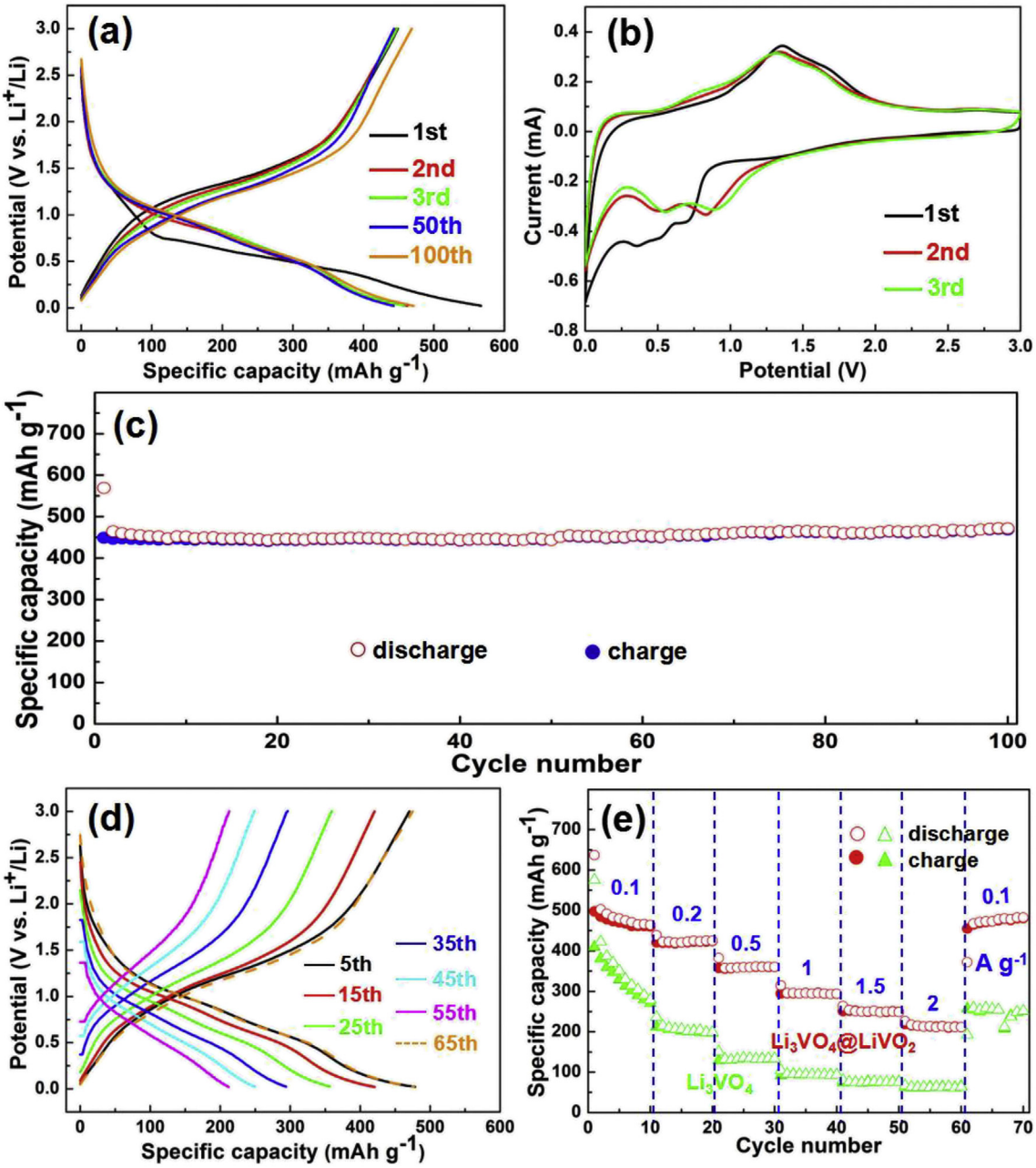

Fig. 4. Electrochemical performance of the Li_3VO_4@$LiVO_2$. (a) The initial three charge and discharge curves. (b) Cyclic voltammograms at a scan rate of 0.2 mV s^{-1}. (c) Capacity retention at a specific current of 0.15 A g^{-1}. (d) Representative charge and discharge curves. (e) Rate capability.

correspond to the lithiation process that can be described as: $xLi^+ + Li_3VO_4 + xe^- \rightarrow Li_{3+x}VO_4$ (x = 3), accompanied by the formation of solid electrolyte interface (SEI) [7–9]. The reduction peaks shift to 0.49 and 0.83 V in the 2nd cathodic scan and 0.54 V and 0.89 V in the 3rd cycle, which can be ascribed to the activation of Li_3VO_4, being similar to that reported in literature [6–8]. The profiles for the initial three anodic scan are similar, showing an oxidation peak near 1.36 V, which is attributed to the delithiation process that can be described as: $Li_{3+x}VO_4 \rightarrow xLi^+ + Li_3VO_4 + xe^-$ (x = 3) [6–8]. The cycling performance of the Li_3VO_4@$LiVO_2$ is shown in Fig. 4(c), delivering initial discharge and charge capacities of 569 and 448 mAh g^{-1}, respectively. The irreversible capacity loss may be mainly attributed to the formation of solid electrolyte interface (SEI) film and electrolyte decomposition [6,21]. Notably, after 100 cycles, the discharge and charge capacity maintain of 471 and 468 mAh g^{-1}. The reversible capacity is lower than the theoretical value (i.e., ~590 mAh g^{-1}), partially due to the relative low specific capacity of $LiVO_2$ (i.e., 200–300 mAh g^{-1}) [19,20]. Apart from the satisfactory cyclability, outstanding rate capability of electrode material is also crucial for the application in LIBs. To estimate the rate capability, the Li_3VO_4@$LiVO_2$ electrode was evaluated at different current densities ranging from 0.1 to 2 A g^{-1}. As shown in Fig. 4(d), along with the increasing of specific current, the discharge potential decreases and the charge potential increases due to enhanced polarization [22]. When reverting the specific current to 0.1 A g^{-1}, the voltage polarization disappears, suggesting highly reversible lithiation/delithiation process. As shown in Fig. 4(e), the discharge capacity steadily decreases as the current density increase, being 473, 421, 356, 295, 251 and 214 mAh g^{-1} at 0.1, 0.2, 0.5, 1, 1.5 and 2 A g^{-1}, respectively. Remarkably, a reversible capacity of 478 mA g^{-1} can be recovered once the current density is reduced back to 0.1 A g^{-1}, which is distinctly improved compared with that of pristine Li_3VO_4.

Reaction kinetics of the Li_3VO_4@$LiVO_2$ were studied to elaborate the superior cyclability and rate performance, in terms of electronic conductivity, lithium ion diffusion and pseudocapacitive contribution. Electrochemical impedance spectroscopy (EIS) spectra of Li_3VO_4@$LiVO_2$ in comparison with pristine Li_3VO_4 are shown in Fig. 5(a). The intercept in high-frequency can be attributed to the contact resistance (Re) caused by SEI film and/or electrolyte, the medium-frequency semicircle is due to the charge-transfer impedance (Rct) on electrode/electrolyte interface, and the inclined line in low-frequency corresponds to the Li-ion diffusion process within electrodes [23]. The kinetic differences of the electrodes were investigated by modeling AC impedance spectra via an R(C(RW)) equivalent circuit. As shown in Table 1, despite little difference for contact resistance (Re) which may be caused by electrode preparation, the Li_3VO_4@$LiVO_2$ electrode delivers much lower charge-transfer resistance (Rct) than pristine Li_3VO_4 electrode. Moreover, powder conductivity measurement indicates that the Li_3VO_4@$LiVO_2$ exhibits much higher interior electrical conductivity than that for pristine Li_3VO_4 (Table 2).

Table 1
Electrode kinetic parameters obtained from equivalent circuit fitting of Nyquist plots.

Electrode	Re(Ω)	Rct(Ω)
Pristine Li_3VO_4	5.65	57.52
$Li_3VO_4/LiVO_2$	2.13	12.25

Table 2
Powder electrical conductivity for the $Li_3VO_4/LiVO_2$ and pristine Li_3VO_4.

Powder	(S cm^{-1})
Pristine Li_3VO_4	8.4816×10^{-10}
$Li_3VO_4/LiVO_2$	4.4761×10^{-6}

In addition to Rct for electrode and electrical conductivity for powder, the lithium ion diffusion coefficient (D) also exhibits synergistic effect on the performance. The values of D were calculated from the inclined lines in the Warburg region using the equation of $D = R^2T^2/2A^2n^4F^4C^2\sigma^2$, where *R* is the gas constant, *T* is the absolute temperature, *A* is the surface area of the cathode electrode, *n* is the number of electrons transferred per molecule, *F* is the Faraday constant, C is the Li^+ concentration, and σ is the Warburg factor associated with Z' ($Z' \propto \sigma\omega^{-1/2}$) [9]. The *D* values for the Li_3VO_4@$LiVO_2$ and pristine Li_3VO_4 were calculated to be 9.05×10^{-15} and 8.58×10^{-16} cm^2 s^{-1} through σ estimated from Fig. 5(b), revealing Li_3VO_4@$LiVO_2$ electrode has faster kinetics than pristine Li_3VO_4 electrode for lithium ions insertion/extraction.

The largely reduced Rct and enhanced lithium ion diffusion in Li_3VO_4@$LiVO_2$ may stem from the synergistic effect between the two phases in the composite. On the one hand, $LiVO_2$ exhibits high electronic conductivity, and the homogeneous hybridization between Li_3VO_4 and $LiVO_2$ can significantly improve the electron transfer within the electrode. On the other hand, the presence of $LiVO_2$ can suppress the growth of Li_3VO_4 crystals, and the smaller

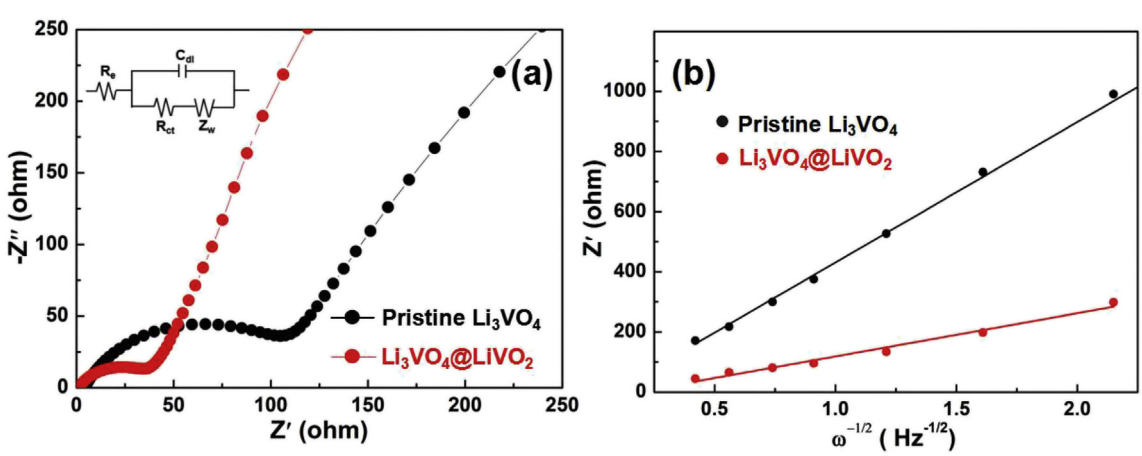

Fig. 5. (a) EIS spectra and (b) variations and fittings between Z' and the reciprocal square root of the angular frequency in the low frequency region for pristine Li_3VO_4 and Li_3VO_4@$LiVO_2$.

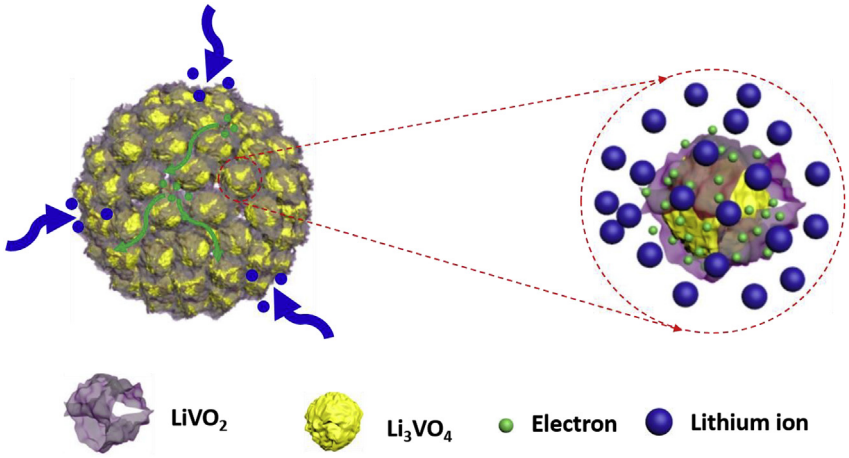

Fig. 6. Schematic advantages for the Li_3VO_4@$LiVO_2$ in terms of electron transmission and lithium ion diffusion.

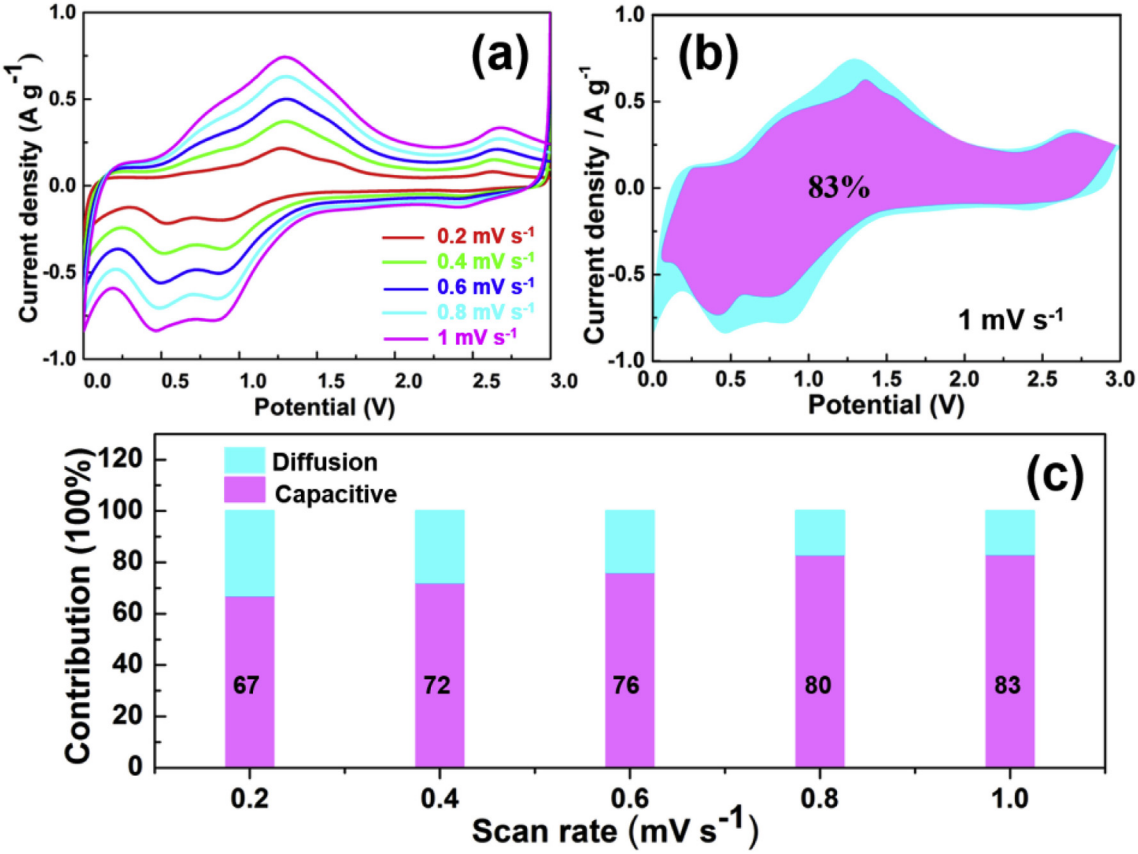

Fig. 7. (a) CV curves at different scanning rate. (b) Corresponding Capacitive (pink) and diffusion-controlled (light blue) contribution to charge storage at 1.0 mV s^{-1}. (c) Normalized contribution ratio of capacitive (pink) and diffusion-controlled (light blue) capacities at different scan rate. (For interpretation of the references to colour in this figure legend, the reader is referred to the Web version of this article.)

the particle size of Li_3VO_4, the higher the lithium ion diffusion. The electrochemical advantages stemming from the specific architecture of the Li_3VO_4@$LiVO_2$ are shown in Fig. 6.

Fig. 7(a) displays CV curves for the Li_3VO_4@$LiVO_2$ at various scan rates from 0.2 to 1 mV s^{-1}, from which the pseudocapacitive contribution for charge storage can be quantitatively quantified. According to the equation of $i(V) = k_1v + k_2v^{1/2}$, the ratios for Li-ion capacitive contribution can be distinguished by separating the k_1v part [24–27]. As shown in Fig. 7(b), a high capacitive contribution of 83% is obtained at a scan rate of 0.8 mV s^{-1}. Even at a slow scan rate of 0.2 mV s^{-1}, pseudocapacitive contribution for charge storage in the Li_3VO_4@$LiVO_2$ electrode can reach 67% (Fig. 7(c)). Generally, high electronic/ionic conductivity for electrode materials are considered as prerequisites to trigger extrinsic pseudocapacitance, which usually necessitates constructing specific architectures and designing especial morphologies at nanoscale dimension [28–30]. In our Li_3VO_4@$LiVO_2$, Li_3VO_4 nanocrystals homogeneously embraced by amorphous $LiVO_2$, which renders high electrical

conductivity and lithium ion diffusion, thus triggering pseudocapacitive contribution for lithium ions storage. As a result, superior rate capability and ultra-stable cycle performance were spontaneously achieved.

4. Conclusions

In summary, it was demonstrated that the performance of Li_3VO_4 anode for LIBs can be significantly improved via feasibly hybridizing $LiVO_2$, with homogeneously distributed $LiVO_2$ acting as both electrical reinforcement and structural regulator. Spontaneously, high electronic conductivity and high lithium ion diffusion are achieved for the Li_3VO_4@$LiVO_2$ composite, which triggers high pseudocapacitive contribution for lithium ion storage, resulting in superior performance. The Li_3VO_4@$LiVO_2$ delivers initial discharge and charge capacities of 569 and 448 mAh g^{-1} at a specific current of 0.15A g^{-1}, which maintain at 468 and 471 mAh g^{-1} after 100 cycles. After 70 cycles at various specific currents from 0.1 to 2.0 A g^{-1}, the discharge and charge capacities of the Li_3VO_4@$LiVO_2$ restore 100% when reverting the specific current to 0.1 A g^{-1}. The facile fabrication method which can be easily scale-up, the intrinsic safety performance and the superior electrochemical performance of the Li_3VO_4@$LiVO_2$ demonstrate great promising for practical application in high-performance LIBs.

Acknowledgement

We gratefully acknowledge the financial support from Natural Science Foundation of China (NSFC 51672158, 51772169, 51572151), open project of State Key Laboratory of Physical Chemistry of Solid Surfaces (201608), and the Outstanding Youth Science and Technology Innovation Team Project of Hubei Educational Committee (T201603).

References

[1] H.D. Yoo, E. Markevich, G. Salitra, D. Sharon, D. Aurbach, On the challenge of developing advanced technologies for electrochemical energy storage and conversion, Mater. Today 17 (2014) 110–121.
[2] M. Armand, J.M. Tarascon, Building better batteries, Nature 451 (2008) 652–657.
[3] A. Manthiram, Materials challenges and opportunities of lithium ion batteries, J. Phys, Chem. Lett. 2 (2011) 176–184.
[4] M.G. Kim, J. Cho, Reversible and high-capacity nanostructured electrode materials for Li-ion batteries, Adv. Funct. Mater. 19 (2009) 1497–1514.
[5] S.B. Ni, J.C. Zhang, J.J. Ma, X.L. Yang, L.L. Zhang, X.M. Li, H.B. Zeng, Approaching the theoretical capacity of Li_3VO_4 via electrochemical reconstruction, Adv. Mater. Interfaces. 3 (2016) https://doi.org/10.1002/admi.201500340 1500340 10p.
[6] S.B. Ni, X.H. Lv, J.J. Ma, X.L. Yang, L.L. Zhang, Electrochemical characteristics of lithium vanadate, Li_3VO_4 as a new sort of anode material for Li-ion batteries, J. Power Sources 248 (2014) 122–129.
[7] Z.Y. Liang, Z.P. Lin, Y.M. Zhao, Y.Z. Dong, Q. Kuang, X.H. Lin, X.D. Liu, D.L. Yan, New understanding of Li_3VO_4/C as potential anode for Li-ion batteries: preparation, structure characterization and lithium insertion mechanism, J. Power Sources 274 (2015) 345–354.
[8] W.T. Kim, Y.U. Jeong, Y.J. Lee, Y.J. Kim, J.H. Song, Synthesis and lithium intercalation properties of Li_3VO_4 as a new anode material for secondary lithium batteries, J. Power Sources 244 (2013) 557–560.
[9] Y. Shi, J.Z. Wang, S.L. Chou, D. Wexler, H.J. Li, K. Ozawa, H.K. Liu, Y.P. Wu, Hollow structured Li_3VO_4 wrapped with graphene nanosheets in situ prepared by a one-pot template-free method as an anode for lithium-ion batteries, Nano Lett. 13 (2013) 4715–4720.
[10] Z.Y. Liang, Y.M. Zhao, L.Z. Ouyang, Y.Z. Dong, Q. Kuang, X.H. Lin, X.D. Liu, D.L. Yan, Synthesis of carbon-coated Li_3VO_4 and its high electrochemical performance as anode material for lithium-ion batteries, J. Power Sources 252 (2014) 244–247.
[11] Z.L. Jian, M.B. Zheng, Y.L. Liang, X.X. Zhang, S. Gheytani, Y.C. Lan, Y. Shi, Y. Yao, Li_3VO_4 anchored graphene nanosheets for long-life and high-rate lithium-ion batteries, Chem. Commun. 51 (2015) 229–231.
[12] Q.D. Li, J.Z. Sheng, Q.L. Wei, Q.Y. An, X.J. Wei, P.F. Zhang, L.Q. Mai, A unique hollow Li_3VO_4/carbon nanotube composite anode for high rate long-life lithium-ion batteries, Nanoscale 6 (2014) 11072–11077.
[13] J. Liu, P.J. Lu, S.Q. Liang, J. Liu, W.J. Wang, M. Lei, S.S. Tang, Q. Yang, Ultrathin Li_3VO_4 nanoribbon/graphene sandwich-like nanostructures with ultrahigh lithium ion storage properties, Nano Energy 12 (2015) 709–724.
[14] S.B. Ni, J.C. Zhang, X.H. Lv, X.L. Yang, L.L. Zhang, Superior electrochemical performance of Li_3VO_4/NiO/Ni electrode via a coordinated electrochemical reconstruction, J. Power Sources 291 (2015) 95–101.
[15] S.B. Ni, X.H. Lv, J.J. Ma, X.L. Yang, L.L. Zhang, The fabrication of Li_3VO_4/Ni composite material and its electrochemical performance as anode for Li-ion battery, Electrochim. Acta 130 (2014) 800–804.
[16] Y.Z. Dong, Y.M. Zhao, H. Duan, P. Singh, Q. Kuang, H.J. Peng, $Li_{2.97}Mg_{0.03}VO_4$: high rate capability and cyclability performances anode material for rechargeable Li-ion batteries, J. Power Sources 319 (2016) 104–110.
[17] Y.Z. Dong, H. Duan, K.S. Park, Y.M. Zhao, Mo^{6+} doping in Li_3VO_4 anode for Li-ion batteries: significantly improve the reversible capacity and rate performance, ACS Appl. Mater. Interfaces 9 (2017) 27688–27696.
[18] L. Chen, X.L. Jiang, N.N. Wang, J. Yue, Y.T. Qian, J. Yang, Surface-amorphous and oxygen-deficient $Li_3VO_{4-\delta}$ as a promising anode material for lithium-ion batteries, Adv. Sci. 2 (2015), 1500090 5p.
[19] X.H. Li, Z. Su, H.L. Tian, Y.H. Zhang, Rhombohedral-structured $LiVO_2$ prepared by a novel two-step method and its electrochemical properties, Int. J. Electrochem. Sci. 12 (2017) 693–698.
[20] A.R. Armstrong, C. Lyness, P.M. Panchmatia, M.S. Islam, P.G. Bruce, The lithium intercalation process in the low-voltage lithium battery anode $Li_{1+x}V_{1-x}O_2$, Nature Mater. 10 (2011) 223–229.
[21] H.Q. Li, X.Z. Liu, T.Y. Zhai, D. Li, H.S. Zhou, Li_3VO_4: a promising insertion anode material for lithium-ion batteries, Adv. Energy Mater. 3 (2013) 428–432.
[22] S.B. Ni, J.J. Ma, X.H. Lv, X.L. Yang, L.L. Zhang, The fine electrochemical performance of porous Cu_3P/Cu and the high energy density of Cu_3P as anode for Li-ion batterie, J. Mater. Chem. A 2 (2014) 20506–20509.
[23] Y.J. Zhu, C.S. Wang, Novel CV for phase transformation electrodes, J. Phys. Chem. C 115 (2010) 823–832.
[24] J. Wang, J. Polleux, J. Lim, B. Dunn, Pseudocapacitive contributions to electrochemical energy storage in TiO_2 (Anatase) nanoparticles, J. Phys. Chem. C 111 (2007) 14925–14931.
[25] V. Augustyn, P. Simon, B. Dunn, Pseudocapacitive oxide materials for high-rate electrochemical energy storage, Energy Environ. Sci. 7 (2014) 1597–1614.
[26] J.L. Liu, J. Wang, C.H. Xu, H. Jiang, C.Z. Li, L.L. Zhang, J.Y. Lin, Z.X. Shen, Advanced energy storage devices: basic principles, analytical methods, and rational materials design, Adv. Sci. (2017), 1700322, 19p.
[27] J.L. Liu, J. Wang, Z.L. Ku, H.H. Wang, S. Chen, L.L. Zhang, J.Y. Lin, Z.X. Shen, Aqueous rechargeable alkaline $Co_xNi_{2-x}S_2/TiO_2$ battery, ACS Nano 10 (2016) 1007–1016.
[28] D.L. Chao, C.R. Zhu, P.H. Yang, X.H. Xia, J.L. Liu, J. Wang, X.F. Fan, S.V. Savilov, J.Y. Lin, H.J. Fa, Z.X. Shen, Array of nanosheets render ultrafast and high-capacity Na-ion storage by tunable pseudocapacitance, Nat. Commun. 7 (2016) 12122.
[29] D.L. Chao, P. Liang, Z. Chen, L.Y. Bai, H. Shen, X.X. Liu, X.H. Xia, Y.L. Zhao, S.V. Savilov, J.Y. Lin, Z.X. Shen, Pseudocapacitive Na-ion storage boosts high rate and areal capacity of self-branched 2D layered metal chalcogenide Nanoarrays, ACS Nano 10 (2016) 10211–10219.
[30] Q. Li, Q. Wei, Q. Wang, W. Luo, Q. An, Y. Xu, C. Niu, C. Tang, L. Mai, Self-template synthesis of hollow shell-controlled Li_3VO_4 as a high-performance anode for lithium-ion batteries, J. Mater. Chem. A 3 (2015) 18839–18842.